PHOTONICS Research

Submicrometer optical frequency combs based on SPPs metallic multi-ring resonators

Zhitao Huang,[1,2] Fangyuan Ma,[1] Keqian Dong,[1,2] Shizhong Yue,[1,2,6] Chao Li,[1,2] Yulin Wu,[1,2] Junhui Huang,[1,2] Xu Han,[3] Jiaqian Sun,[1,2] Zhaofeng Li,[4] Kong Liu,[1,2] Zhijie Wang,[1,2,7] Yong Lei,[5,8] Shengchun Qu,[1,2] and Zhanguo Wang[1,2]

[1]Key Laboratory of Semiconductor Materials Science, Beijing Key Laboratory of Low Dimensional Semiconductor Materials and Devices, Institute of Semiconductors, Chinese Academy of Sciences, Beijing 100083, China
[2]Center of Materials Science and Optoelectronics Engineering, University of Chinese Academy of Sciences, Beijing 100049, China
[3]School of Integrated Circuits and Electronics, MIIT Key Laboratory for Low-Dimensional Quantum Structure and Devices, Beijing Institute of Technology, Beijing 100081, China
[4]Engineering Research Center for Semiconductor Integrated Technology, Institute of Semiconductors, Chinese Academy of Sciences, Beijing 100083, China
[5]Fachgebiet Angewandte Nanophysik, Institut für Physik & IMN MacroNano, Technische UniversitätIlmenau, Ilmenau 98693, Germany
[6]e-mail: yueshizhong@semi.ac.cn
[7]e-mail: wangzj@semi.ac.cn
[8]e-mail: yong.lei@tu-ilmenau.de

Received 20 February 2023; revised 3 July 2023; accepted 3 July 2023; posted 14 August 2023 (Doc. ID 488160); published 24 November 2023

Optical frequency combs (OFCs) have great potential in communications, especially in dense wavelength-division multiplexing. However, the size of traditional OFCs based on conventional optical microcavities or dispersion fibers is at least tens of micrometers, far larger than that of nanoscale electronic chips. Therefore, reducing the size of OFCs to match electronic chips is of necessity. Here, for the first time to our knowledge, we introduce surface plasmon polaritons (SPPs) to the construction of OFCs to realize a miniature device. The thickness of our device is reduced below 1 μm. Though the presence of SPPs may induce ohmic and scattering loss, the threshold of the device is obtained as 9 μW, comparable to the conventional device. Interestingly, the response time is 13.2 ps, much faster than the optical counterparts. This work provides a feasible strategy for the miniaturization of OFCs.

https://doi.org/10.1364/PRJ.488160

1. INTRODUCTION

Optical frequency combs (OFCs) have played an important role in the field of metrology, promoting the progress of precision time measurement and spectroscopy [1]. However, its application prospects in more expansive fields, such as communications, have not been fully developed [2–4]. The use of dense wavelength division multiplexing (DWDM) is an effective means to improve communication capacity [5], but each channel needs to use lasers with different wavelengths and the vast and expensive discrete wavelength laser source arrays hinder DWDM from entering thousands of households [6]. Correspondingly, OFCs with multiple equidistant peaks could solve this problem properly. Compared with multiple lasers, the stable wavelength spacing and stronger anti-interference ability of such OFCs are more conducive to the design of optical add–drop multiplexers and other components [7]. Moreover, the single device is more suitable for developing integrated optoelectronics in terms of low energy consumption and the convenience of system integration. These advantages facilitate the application of OFCs in the communication field, especially in on-chip interconnection [8,9].

The miniaturization and integration of OFCs are crucial factors for their practical application in the communication field. Zinner *et al.* initially realized OFCs through external frequency mixing of a series of large femtosecond lasers [2]. Jones *et al.* further developed a method to obtain OFCs through a single mode-locked laser [4]. Because these devices are huge and expensive, the systems can only be used in advanced scientific fields such as high-precision time measurement and high-resolution spectral analysis. In order to realize the miniaturization of OFCs, methods using dispersion fiber and high-quality-factor microcavity were gradually proposed [7,10–14]. The microcavity approach can only realize micrometer OFCs, still larger than the size of currently used communication lasers, and soliton combs are usually very inefficient [15]. It is worth noting that the microcavity method based on Kerr nonlinearity usually needs ultra-high quality factors to enhance the optical field intensity, improve the third-order nonlinear efficiency, and

finally obtain OFCs based on four-wave mixing [16–19]. However, in order to obtain the ultra-high quality factor, the current microcavity OFCs demand a nearly perfect microcavity structure to reduce the mode volume and light leakage. A perfect microcavity necessitates an ultra-smooth and regular surface, and needs to be suspended in a uniform medium, which places extremely high requirements on the processing technology [7,20]. These difficulties make their prospects for on-chip integration vague. Fortunately, surface plasmon polaritons (SPPs), which can compress wavelength and localize the light field, have made many breakthroughs in miniaturizing lasers. The compression effect on the wavelength enables the device to break through the diffraction limit, thus reaching the nanometer scale to match the size of current electronic chips [21–26]. When the light field is localized near the metal–dielectric interface, the peak light intensity is greatly increased. Thus, the threshold of OFCs based on third-order nonlinear effects would be lowered. Therefore, introducing SPPs to microcavities to solve the dilemma of OFC miniaturization would be feasible.

In this paper, we propose an implementation of submicrometer OFCs based on metallic multi-ring (MMR) resonators. Reducing the device thickness and enhancing the local light field are realized simultaneously via the whispering gallery cavity with the SPP waveguide. In addition, the approximately quarter phase-shifted distributed feedback Bragg (DFB) cavity formed along the radial direction can allow the light field to superimpose near the center of the circle, thus obtaining ultra-high light intensity and enhancing the third-order nonlinear effect. The threshold of OFCs is only 9 μW, which is comparable to that of traditional microcavity OFCs. Through controlled dual-pump time-resolved fluorescence spectroscopy experiments with nanosheet optical-mode lasers, we found that OFCs had much faster dynamics than photon-mode lasers, suggesting that the introduction of SPPs is efficacious.

2. METHOD AND CHARACTERIZATION

A. Construction of Metallic Multi-Ring

Electron beam glue (Allrisist E-Beam Resist AR-P 671.05) was first spin-coated on the cleaned quartz substrate at 4000 r/min for 1 min, baked at 150°C for 3 min, and then the conductive glue (Allrisist E-Beam AR-PC 5090.02) was spin-coated at 2000 r/min for 1 min. Electron beam exposure was performed at a dose of 120 $\mu C \cdot cm^{-2}$ on Raith e-LiNE plus high-resolution electron beam lithography system. The sample was developed by a mixture of methyl isobutyl ketone (Sinopharm Chemical) and isopropanol (Sinopharm Chemical). Gold film with 50 nm thickness was deposited by thermal evaporation, and a lift-off process was performed to achieve MMR. After cleaning by acetone, 5 nm aluminum oxide was obtained with atomic layer deposition.

B. Perovskite Nanosheet Growth

Perovskite nanosheets were obtained by anti-solvent assisted crystallization [27]. The sapphire substrate was first pretreated with ozone for 10 min, and then the prepared PDMS sheet was tightly attached to the substrate to form a confined growth environment. After that, the precursor of $CsPbBr_3$ (5 μL, 0.2 mol/L) was dropped on the substrate. The synergistic effect of capillary force and diffusion drove the solution to creep into the gap between PDMS and the substrate, and finally a nanosheet was obtained. During the growth of the nanosheet, the sample was placed in a beaker containing acetonitrile, an anti-solvent. After 24 h, the solvent in the precursor was completely evaporated, and the PDMS sheet was mechanically peeled off. Perovskite nanosheets were on the substrate.

C. Construction of OFCs

OFCs were constructed by the mechanical transfer method. The perovskite nanosheets were adsorbed by PDMS, aligned and attached to the gold ring resonator under an optical microscope, and desorbed by heating to obtain the OFC sample [28].

D. Finite Element Simulation Setup

The simulation model adopted a two-dimensional axisymmetric model, and the structure size was consistent with that of the experimental sample. Since the perovskite nanosheets were large enough to completely cover the resonant cavity and the SPP wavelength was much smaller than the device size, the two-dimensional nanosheets and substrate were considered as infinite in the study. The boundary condition was set as a scattering boundary condition, and a perfectly matched layer was set as an absorbent layer. Considering that the aluminum oxide layer was too thin and completely covered the resonant cavity, it was set as a transition layer to simplify the model.

E. Structure Characterization

Optical microscopy images were taken with an Olympus BX53M microscope with a 50× objective lens (NA = 0.8). The scan area was 5 μm × 5 μm with a scan rate of 1 Hz. 1024 points per line and 1024 lines per image were used for data sampling on a Bruker Dimension Edge. Electron micrographs of the surface and cross-sections of the MMR were obtained by the FB-2100 focused ion beam (FIB) system.

F. Optical Measurements

Normal time-resolved fluorescence spectroscopy was performed using an Edinburgh Instrument FLS1000. Steady-state fluorescence spectroscopy was performed using a Varian Cary Eclipse.

The dual-pump time-resolved fluorescence spectroscopy experiment was completed based on a homemade test system. The laser source had a wavelength of 800 nm, a repetition rate of 1 kHz, and a pulse width of 40 fs. The laser wavelength of 400 nm was obtained through a BBO frequency doubling crystal as a pump light source. The pump light source was focused on the sample by an Olympus magnification 5× (NA = 0.1) polarization maintaining lens to ensure complete coverage of the sample. The fluorescence was also collected by this objective lens and transmitted to the spectrometer (Princeton Instruments, Acton SP2300i, with 1200 mm^{-1} grating), and the test data were obtained by liquid nitrogen cooling CCD (Princeton Instruments, Pylon camera). Test-related light paths are shown in the appendix.

3. RESULTS AND DISCUSSION

Microcavity OFCs are usually related to the third-order nonlinear effect of gain materials. First, the annihilation of intrinsic photons produces signal and idler photons, and then they

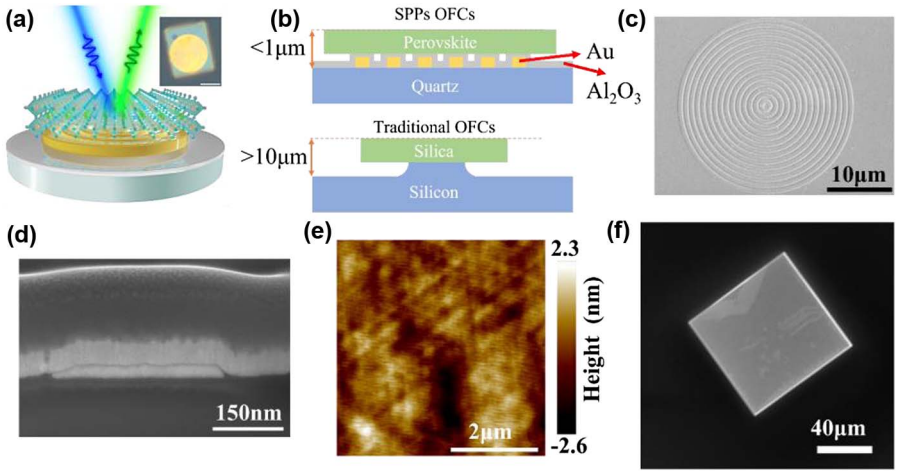

Fig. 1. (a) 3D schematic diagram of OFC device; the inset is the optical photo of the real device. (b) Comparison schematic diagram of the cross section along the center of the circle. (c) SEM image of the metallic ring resonator. (d) SEM image of a single ring section; contrast image obtained by depositing metallic platinum by FIB. (e) AFM scan image of the metal on quartz by the same deposition process showing a surface roughness of RMS = 0.6 nm. (f) SEM image of perovskite nanosheets.

undergo four-wave mixing with intrinsic photons to produce more spectral comb lines. Ultimately an OFC is generated [29]. The efficiency of these third-order nonlinear processes is proportional to the optical field strength. Therefore, improving the light field intensity is the core of the device structure design. In addition, to meet the phase-matching condition, the negative free spectral range (FSR) caused by microcavity dispersion should be compensated by positive anomalous dispersion of the material. For SPP, only TM modes can exist, whose dispersion relation is given by the equation [30]

$$\frac{\beta}{k} \approx \sqrt{\frac{\varepsilon_1 \cdot \varepsilon_2}{\varepsilon_1 + \varepsilon_2}},$$

where ε_1 and ε_2 are the dielectric constants of the gold film [31] and perovskite material [32]. The Au film and perovskite dielectric constant were fitted by the Drude model [33] and Sellmeier equation [34], respectively, and the dispersion function of SPP was obtained. Thus, we can calculate the group velocity dispersion of SPP. According to this analysis, we confirm that SPP can compensate for the negative structural dispersion of the microcavity, making FSR > 0. Therefore, when the cavity mode is coupled with the frequency conversion, OFCs can be generated.

To increase the light intensity in the gain material, we designed the device structure as shown in Figs. 1(a) and 1(b). The device consists of concentric MMR constructed on a quartz substrate, an insulating dielectric layer of aluminum oxide covering the MMR, and a gain layer of perovskite nanosheets. The inner diameter of the innermost ring is 350 nm, the width of each metal ring is 350 nm, and the ring spacing is also 350 nm. There are 15 rings with a thickness of 50 nm, as shown in Figs. 1(c) and 1(d). For the innermost metal ring, a whispering gallery resonator based on SPP waveguides can be realized. Along the radial direction, the metal ring arrays distributed periodically form an approximate DFB cavity. In order to reduce the ohmic loss of the metal, a 5 nm aluminum oxide insulating layer is deposited on the MMR, and the perovskite nanosheet is closely attached to the upper surface of the MMR resonator. As shown in Fig. 1(c), the MMR structure is complete, and the metal film's root mean square (RMS) obtained by the deposition process is 0.6 nm in Fig. 1(e). Thus, the transferred perovskite nanosheets can be well attached to the MMR, reducing the scattering loss. The size of the perovskite nanosheets is larger than that of the MMR resonator and completely covers the resonator. Figure 1(f) shows the SEM image of the perovskite nanosheets. The thickness of the entire device except the substrate is less than 1 μm, which is smaller than the microcavity OFCs at visible light reported so far.

A seven-line OFC was obtained when the device was excited by a 14.8 μW femtosecond laser (the wavelength is 400 nm). As shown in Fig. 2(a), the center wavelength of the OFC is 541 nm and the wavelength spacing is 0.98 nm. The central wavelength is consistent with the intrinsic laser wavelength of the perovskite, and the wavelength spacing corresponds to one or more FSRs, determined by the dispersion of the material and the cavity structure [35]. Considering the multi-whispering gallery mode of this device, there may be unequal FSR caused by the dispersion difference of multiple cavity modes. However, for the case close enough to the eigenmodes, the error accumulated in the FSR is small enough. In Fig. 2(a), there are actually seven comb lines, and the standard deviation of wavelength spacing is negligible (<0.05 nm). Therefore, the discrete wavelength light sources obtained are OFCs.

For a steady-state microcavity, FSR is determined by the frequency difference between the two higher-order modes of the microcavity [36],

$$\mathrm{FSR} = \Delta\lambda = -\frac{2\pi}{L}\left(\frac{\partial\beta}{\partial\lambda}\right)^{-1},$$

while FSR for the plasmonic ring structure is

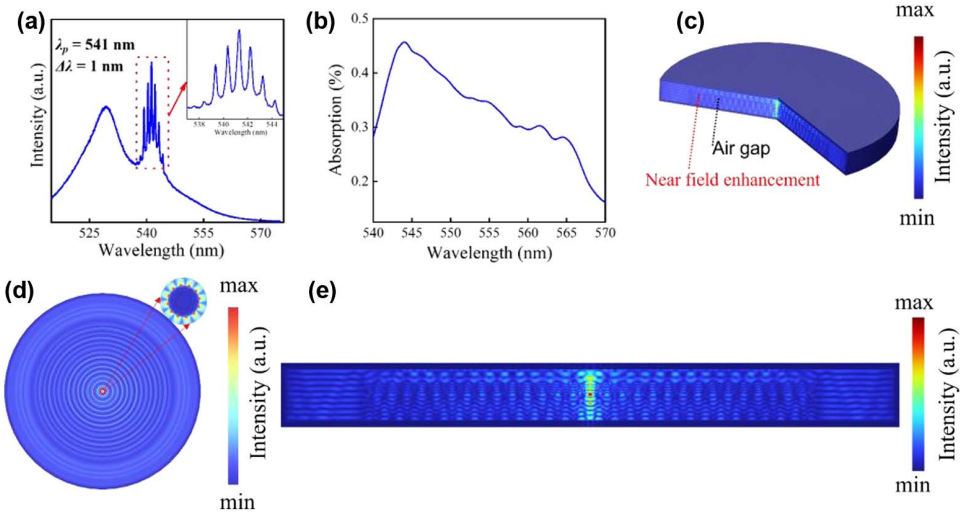

Fig. 2. (a) OFCs spectral pattern with seven comb lines. (b) Simulated absorption spectrum of MMR resonator; the absorption peak is located at 544 nm, which is close to the lasing peak at 541 nm. (c) Simulated electric field distribution of three-dimensional structure at 541 nm. (d) Top view of simulated electric field distribution at the interface of Al_2O_3/Au at 541 nm; the inset shows the light field distribution of one mode in the whispering gallery mode cavities near the innermost ring. (e) Simulated electric field distribution along a section passing through the axis of symmetry at 541 nm.

$$\mathrm{FSR} \approx \frac{\lambda^2}{L}\sqrt{\frac{\varepsilon_1+\varepsilon_2}{\varepsilon_1\cdot\varepsilon_2}},$$

where L is the circumference of the ring. The innermost metal ring's FSR is 1.3 nm, which is close to the result of 0.98 nm. Obviously, in this device, there is only one FSR between two comb lines. For the optical mode, the FSR of the micro-disk can be obtained according to the equation

$$\mathrm{FSR} = \Delta\lambda = -\frac{2\pi}{L}\left(\frac{\partial\beta}{\partial\lambda}\right)^{-1} \approx \frac{\lambda^2}{n_g L}.$$

When the size of the micro-disk is the same as the innermost metal ring, its FSR is 10.0 nm. The comparison results demonstrate that the introduction of SPP is beneficial to reduce the spacing of comb lines and increase the number of comb lines.

In order to explore the interaction between the MMR resonator and the gain medium, we performed finite element simulations using the simulation software COMSOL Multiphysics. The results are shown in Figs. 2(b)–2(e). As shown in Fig. 2(b), the simulated absorption peak is located at 544 nm. Considering the processing accuracy, the error with the lasing peak position is within the acceptable range. As shown in Fig. 2(c), the electric field distribution is concentrated near the metallic rings, weakens along the vertical direction, and concentrates in the central region. The electric field distribution along the metallic ring can be clearly seen in Fig. 2(d); the inset shows the light field distribution of one mode in the whispering gallery cavities near the innermost ring. Apparently, the MMR forms a distinct whispering gallery mode resonator in the direction along the innermost ring, thus providing a standing-wave feedback condition for lasing. In addition, along the radial direction, MMR approximately constitutes a quarter-phase-shifted DFB mode resonator. In Fig. 2(e), it can be seen more clearly that the electric field distribution along the radial direction presents noticeable periodic enhancement and weakening, with an obvious maximum near the center of the circle, similar to the optical field distribution of a DFB cavity [37–39]. As a result of the coupling of these cavity modes, the optical field is superimposed near the center of the circle to generate high field strength and further improve the nonlinear efficiency. Thus, the OFCs based on four-wave mixing were obtained with SPP mode.

The performance of the microcavity structure was investigated by testing the lasing threshold of OFCs. As shown in Fig. 3(a), only the fluorescence peak appears at 527 nm at low pump power. As the pump power increases to 9.83 μW, the lasing peak starts to appear, and the number of comb lines gradually increases as the pump light intensity increases. When the pump power reaches 15 μW, the gain material burns out and the intensity begins to decrease. As shown in Fig. 3(b), the laser threshold is about 9 μW, comparable to the lasing threshold of traditional microcavity OFCs [25,40–43]. Generally, the ohmic loss of SPPs induces a high threshold, but the threshold of the OFC we proposed still maintains a low value.

In addition, introducing SPP MMR resonators to the microcavity can reduce the quality requirement for the OFCs, thus making it easier to obtain the OFCs. Traditional microcavities need quality factor up to millions to achieve OFCs, while in our case, the quality factor of 1974 is sufficient to acquire OFCs. As shown in Fig. 3(c), an optical whispering gallery mode laser constituted by the perovskite nanosheets on the quartz can only obtain single longitudinal-mode lasing rather than OFCs. In particular, with the increase of the pump power, the position of the lasing peak has a slight redshift, because the thermal effect originating from pump power induces the lattice constant increase, and thus the bandgap narrows. Correspondingly, as the pump power increases, the position of the lasing peak has a slight blueshift in the OFC device constituted by the perovskite

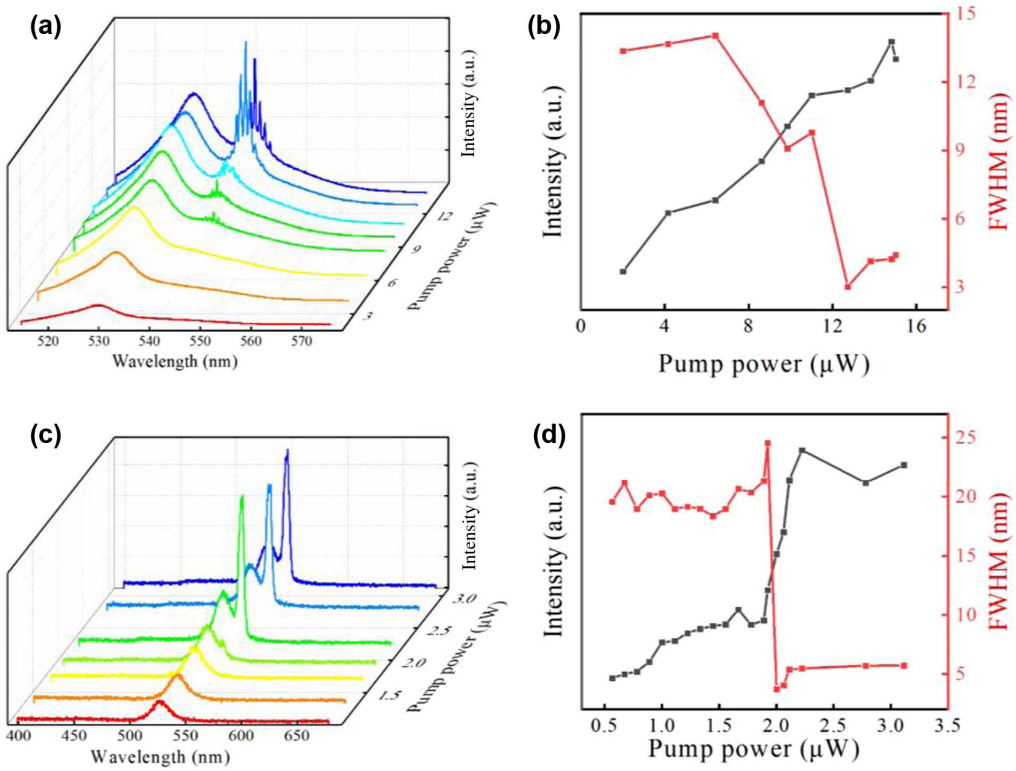

Fig. 3. (a) Fluorescence spectra of OFC devices with excitation power from 2 to 15 μW. The fluorescence peak is located at 527 nm, the lasing peak is located at 541 nm, and the comb lines spread out to both sides with the lasing peak as the center. (b) Integrated emission intensity (black) and FWHM (full-width at half-maximum) (red) of OFCs as a function of pump energy density. The lasing threshold is located at about 9 μW. (c) Fluorescence spectra of perovskite nanosheets. (d) Power-dependent profiles of integrated intensity (black) and FWHM (red) of the nanosheets on quartz around the mode peak 541 nm. The lasing threshold is located at about 1.9 μW.

nanosheets on the MMR, because increasing the resonance energy of the lower polarization branch increases the corresponding wave vector in the dispersion curve, eventually leading to the blueshift of the lasing peak. This proves that the presence of the SPP MMR resonator plays a decisive role in the generation of OFC signal.

To further verify the role of SPP in the generation of OFCs, we performed a control experiment of dual-pump time-resolved fluorescence [44–48]. The intensities of the two pump lights are both set to 95% of the threshold to ensure that lasing can occur when the arrival time of the two beams is close. As shown in Fig. 4, the zero-delay time is at 0.96 ns. When the arrival time of the pump light beams is consistent, perovskite nanosheets exhibit strong lasing peaks. However, when the arrival time difference between the two beams of light becomes large, the intensity of the lasing peak decreases rapidly, and finally only the fluorescence peak remains. Based on this method, the results of dual-pump time-resolved fluorescence of the OFCs and perovskite nanosheet laser on quartz are shown in Figs. 5(a) and 5(b). As shown in Fig. 5(a), the two lifetimes of the OFC device based on double exponential fitting are 13.2 ps (τ_1) and 1.39 ns (τ_2). The longer lifetime of 1.39 ns corresponds to the direct recombination channel of interband transition, while the shorter lifetime of 13.2 ps corresponds to the recombination channel through SPPs. The perovskite nanosheets on the quartz substrate exhibit a

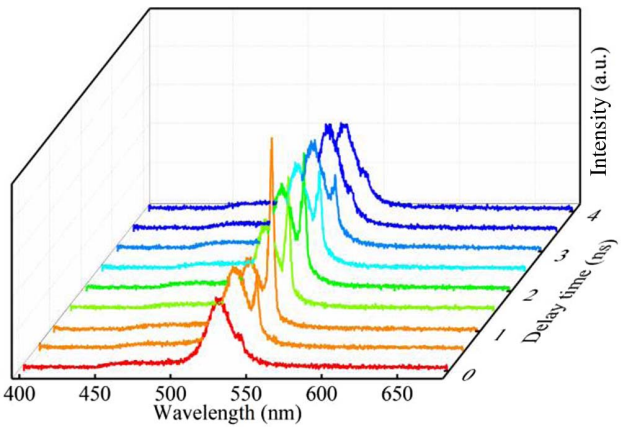

Fig. 4. Waterfall diagram of the lasing peak intensity of perovskite nanosheets changing with the delay time; the intensity of the two pump lights is $0.95P_{th}$.

fluorescence lifetime of 2.25 ns (τ_{lasing}) by single exponential fitting, which corresponds to the direct recombination channel of interband transition in stimulated radiation. Correspondingly, the time-resolved fluorescence spectrum of the perovskite nanosheets is shown in Fig. 5(c), and the lifetime obtained by single-exponential fitting is 11 ns (τ_{SPE}), which

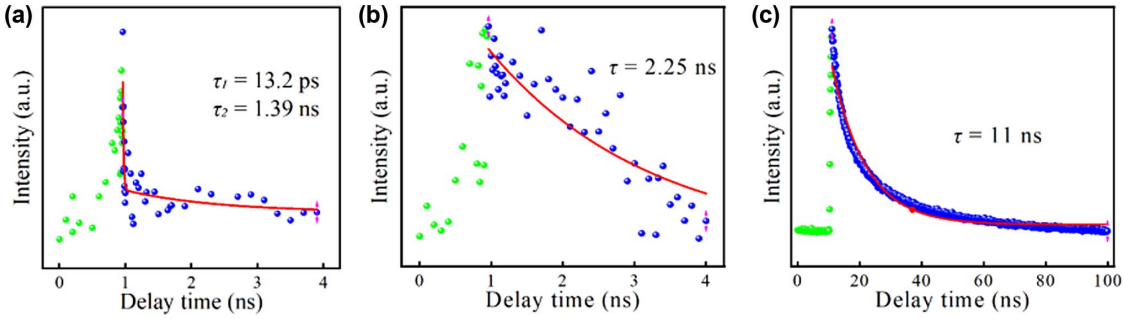

Fig. 5. Dual pump fluorescence lifetime curve for OFCs based on (a) ultrathin MMR nanoresonator and (b) perovskite nanosheet on quartz. (c) Time-resolved fluorescence spectra of perovskite materials.

corresponds to the direct recombination channel of interband transition in spontaneous emission. Comparing τ_{SPE} with τ_{lasing}, stimulated emission can greatly reduce the carrier relaxation time, which is consistent with the lasing dynamics of conventional nanosheet lasers [49]. Comparing τ_{lasing} with τ_2, the stimulated radiation rate of interband recombination is increased, because the spontaneous emission rate will increase at higher pump power. Compared with τ_{lasing}, τ_1 is significantly reduced by two orders of magnitude. Thus, it corresponds to the recombination channel through SPPs, which is also consistent with ordinary SPP lasers [24,50,51]. This also shows that the OFCs benefitting from the MMR resonator obtain a much smaller mode volume and higher Purcell factor, and therefore a much shorter fluorescence lifetime, which is also consistent with the conclusion of the previous simulation. Consequently, it is proved that we have successfully introduced SPPs into the field of OFC generation, which is the reason for the device size reduction.

4. CONCLUSIONS

In summary, we propose a scheme to realize submicrometer OFCs by introducing the surface plasmon polariton waveguide through the MMR. Compared with conventional microcavity OFC devices, the obtained OFCs are less than 1 μm in thickness and less than 10 μW in threshold without the need for suspended microcavities. Therefore, the device can be encapsulated by the current semiconductor process, and has broad application prospects in photoelectric fusion and integrated communication.

APPENDIX A

Figure 6 is the relevant characterization of the fluorescent gain material used in this sample. The material is $CsPbBr_3$ perovskite single-crystal nanosheets. Figure 6(a) is the optical photograph of the sample, showing that the perovskite nanosheets have a complete structure and are easy to transfer. Figure 6(b) is the steady-state fluorescence spectrum of the perovskite material, showing that the fluorescence peak is located at 527 nm, which is consistent with the position of the fluorescence peak in the OFC device, and the width of the fluorescence peak reaches 36 nm, covering the entire frequency band of OFCs. Figure 6(c) is the X-ray diffraction (XRD) image of the perovskite material. There are only two strong characteristic peaks, located at 15.4° and 30.8° and corresponding to (110) and (220) crystal planes, indicating that the material has a relatively good single crystal.

APPENDIX B

Figure 7 shows the optical path used in the optical test. By switching the beam splitters BS1 and BS2, the steady-state fluorescence optical path and the dual-pump time-resolved fluorescence optical path can be switched to ensure the consistency of the same sample lasing threshold and fluorescence dynamics during the test. Time-resolved fluorescence is constructed based on the principle of dual-pump time response. The resolution is determined by the step length of the optical delay line (ODL). The step size is 50 μm, the time resolution is 32.2 fs, and the maximum delay distance is twice as long as the ODL, which is 1200 mm, and thus the maximum delay time is 4 ns.

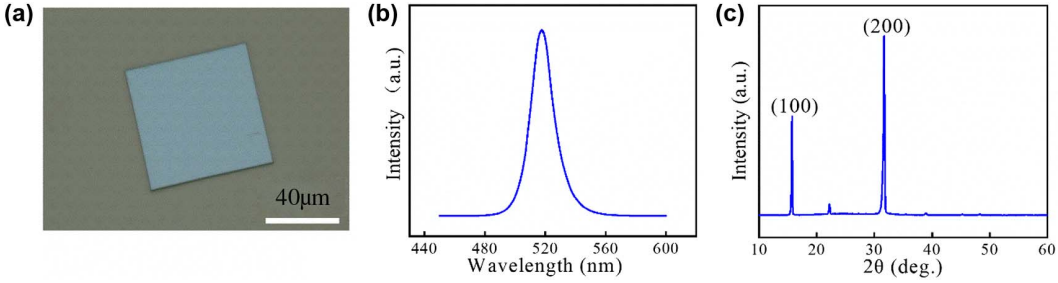

Fig. 6. (a) Optical micrograph of perovskite nanosheet, scale bar 40 μm. (b) Steady-state fluorescence spectrum of perovskite materials. (c) XRD profile of perovskite materials.

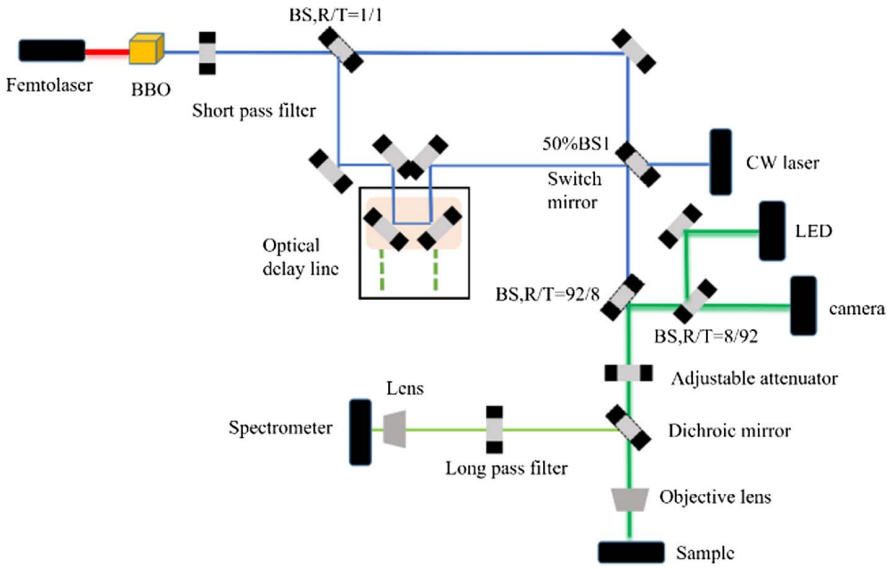

Fig. 7. Schematic diagram of the multiplexing optical path of the dual-pump time-resolved test optical path and variable pump power fluorescence test optical path.

Funding. National Key Research and Development Program of China (2018YFE0204000); Strategic Priority Research Program of the Chinese Academy of Sciences (XDB43000000); National Natural Science Foundation of China (21975245, 51972300, 62274155, U20A20206); Youth Innovation Promotion Association of the Chinese Academy of Sciences (2020114); Beijing Nova Program (2020117).

Acknowledgment. Prof. K. L. appreciates the support from the Youth Innovation Promotion Association.

Disclosures. The authors declare no conflicts of interest.

Data Availability. Data underlying the results presented in this paper are not publicly available at this time but may be obtained from the authors upon reasonable request.

REFERENCES

1. S. A. Diddams, K. Vahala, and T. Udem, "Optical frequency combs: coherently uniting the electromagnetic spectrum," Science **369**, eaay3676 (2020).
2. H. Schnatz, B. Lipphardt, J. Helmcke, F. Riehle, and G. Zinner, "First phase-coherent frequency measurement of visible radiation," Phys. Rev. Lett. **76**, 18–21 (1996).
3. J. Reichert, M. Niering, R. Holzwarth, M. Weitz, T. Udem, and T. W. Hänsch, "Phase coherent vacuum-ultraviolet to radio frequency comparison with a mode-locked laser," Phys. Rev. Lett. **84**, 3232–3235 (2000).
4. S. A. Diddams, D. J. Jones, J. Ye, S. T. Cundiff, J. L. Hall, J. K. Ranka, R. S. Windeler, R. Holzwarth, T. Udem, and T. W. Hänsch, "Direct link between microwave and optical frequencies with a 300 THz femtosecond laser comb," Phys. Rev. Lett. **84**, 5102–5105 (2000).
5. J. Yu and X. Zhou, "Ultra-high-capacity DWDM transmission system for 100G and beyond," IEEE Commun. Mag. **48**, S56–S64 (2010).
6. R. Antil and S. B. Pinki, "An overview of DWDM technology & network," Int. J. Sci. Technol. Res. **1**, 43–46 (2012).
7. H. Hu and L. K. Oxenløwe, "Chip-based optical frequency combs for high-capacity optical communications," Nanophotonics **10**, 1367–1385 (2021).
8. S. Papaioannou, D. Fitsios, G. Dabos, K. Vyrsokinos, G. Giannoulis, A. Prinzen, C. Porschatis, M. Waldow, D. Apostolopoulos, H. Avramopoulos, and N. Pleros, "On-chip dual-stream DWDM eight-channel-capable SOI-based MUXs/DEMUXs with 40-GHz channel bandwidth," IEEE Photon. J. **7**, 7900210 (2015).
9. J. Ahn, M. Fiorentino, R. G. Beausoleil, N. Binkert, A. Davis, D. Fattal, N. P. Jouppi, M. McLaren, C. M. Santori, R. S. Schreiber, S. M. Spillane, D. Vantrease, and Q. Xu, "Devices and architectures for photonic chip-scale integration," Appl. Phys. A **95**, 989–997 (2009).
10. M. Zhang, B. Buscaino, C. Wang, A. Shams-Ansari, C. Reimer, R. Zhu, J. M. Kahn, and M. Loncar, "Broadband electro-optic frequency comb generation in a lithium niobate microring resonator," Nature **568**, 373–377 (2019).
11. P. Del'Haye, A. Schliesser, O. Arcizet, T. Wilken, R. Holzwarth, and T. J. Kippenberg, "Optical frequency comb generation from a monolithic microresonator," Nature **450**, 1214–1217 (2007).
12. M. Piccardo, B. Schwarz, D. Kazakov, M. Beiser, N. Opacak, Y. Wang, S. Jha, J. Hillbrand, M. Tamagnone, W. T. Chen, A. Y. Zhu, L. L. Columbo, A. Belyanin, and F. Capasso, "Frequency combs induced by phase turbulence," Nature **582**, 360–364 (2020).
13. G. A. Sefler, "Frequency comb generation by four-wave mixing and the role of fiber dispersion," J. Lightwave Technol. **16**, 1596–1605 (1998).
14. S. A. Diddams, "The evolving optical frequency comb [Invited]," J. Opt. Soc. Am. B **27**, B51–B62 (2010).
15. Z. Qi, A. Leshem, J. A. Jaramillo-Villegas, G. D'Aguanno, T. F. Carruthers, O. Gat, A. M. Weiner, and C. R. Menyuk, "Deterministic access of broadband frequency combs in microresonators using cnoidal waves in the soliton crystal limit," Opt. Express **28**, 36304–36315 (2020).
16. T. Fortier and E. Baumann, "20 years of developments in optical frequency comb technology and applications," Commun. Phys. **2**, 153 (2019).
17. T. J. Kippenberg, R. Holzwarth, and S. A. Diddams, "Microresonator-based optical frequency combs," Science **332**, 555–559 (2011).
18. A. Coillet, Z. Qi, I. V. Balakireva, G. Lin, C. R. Menyuk, and Y. K. Chembo, "On the transition to secondary Kerr combs in whispering-gallery mode resonators," Opt. Lett. **44**, 3078–3081 (2019).
19. Z. Qi, G. D'Aguanno, and C. R. Menyuk, "Nonlinear frequency combs generated by cnoidal waves in microring resonators," J. Opt. Soc. Am. B **34**, 785–794 (2017).

20. A. S. Rogov and E. E. Narimanov, "Nonlinear optics at low powers: alternative mechanism of on-chip optical frequency comb generation," Phys. Rev. A **94**, 063832 (2016).
21. D. J. Bergman and M. I. Stockman, "Surface plasmon amplification by stimulated emission of radiation: quantum generation of coherent surface plasmons in nanosystems," Phys. Rev. Lett. **90**, 027402 (2003).
22. R. F. Oulton, V. J. Sorger, T. Zentgraf, R. M. Ma, C. Gladden, L. Dai, G. Bartal, and X. Zhang, "Plasmon lasers at deep subwavelength scale," Nature **461**, 629–632 (2009).
23. M. A. Noginov, G. Zhu, A. M. Belgrave, R. Bakker, V. M. Shalaev, E. E. Narimanov, S. Stout, E. Herz, T. Suteewong, and U. Wiesner, "Demonstration of a spaser-based nanolaser," Nature **460**, 1110–1168 (2009).
24. L. Xu, F. Li, Y. Liu, F. Yao, and S. Liu, "Surface plasmon nanolaser: principle, structure, characteristics and applications," Appl. Sci. **9**, 861 (2019).
25. A. F. Koenderink, "Plasmon nanocavity array lasers: cooperating over losses and competing for gain," ACS Nano **13**, 7377–7382 (2019).
26. C. Li, J. Li, Y. Huang, J. Liu, M. Ma, K. Liu, C. Zhao, Z. Wang, S. Qu, L. Zhang, H. Han, W. Deng, and Z. Wang, "Recent development in electronic structure tuning of graphitic carbon nitride for highly efficient photocatalysis," J. Semicond. **43**, 021701 (2022).
27. L. Zhu, H. Zhang, Q. Lu, Y. Wang, Z. Deng, Y. Hu, Z. Lou, Q. Cui, Y. Hou, and F. Teng, "Synthesis of ultrathin two-dimensional organic–inorganic hybrid perovskite nanosheets for polymer field-effect transistors," J. Mater. Chem. C **6**, 3945–3950 (2018).
28. T. Nisar, T. Balster, and V. Wagner, "Mechanical transfer of electrochemically grown molybdenum sulfide layers to silicon wafer," J. Appl. Electrochem. **51**, 1279–1286 (2021).
29. L. Chang, S. Liu, and J. E. Bowers, "Integrated optical frequency comb technologies," Nat. Photonics **16**, 95–108 (2022).
30. W. L. Barnes, A. Dereux, and T. W. Ebbesen, "Surface plasmon subwavelength optics," Nature **424**, 824–830 (2003).
31. D. I. Yakubovsky, A. V. Arsenin, Y. V. Stebunov, D. Y. Fedyanin, and V. S. Volkov, "Optical constants and structural properties of thin gold films," Opt. Express **25**, 25574–25587 (2017).
32. G. Ermolaev, A. P. Pushkarev, A. Zhizhchenko, A. A. Kuchmizhak, I. Iorsh, I. Kruglov, A. Mazitov, A. Ishteev, K. Konstantinova, D. Saranin, A. Slavich, D. Stosic, E. S. Zhukova, G. Tselikov, A. Di Carlo, A. Arsenin, K. S. Novoselov, S. V. Makarov, and V. S. Volkov, "Giant and tunable excitonic optical anisotropy in single-crystal halide perovskites," Nano Lett. **23**, 2570–2577 (2023).
33. M. Dressel and M. Scheffler, "Verifying the Drude response," Ann. Phys. **518**, 480–544 (2006).
34. G. Ghosh, "Sellmeier coefficients and dispersion of thermo-optic coefficients for some optical glasses," Appl. Opt. **36**, 1540–1546 (1997).
35. A. Pasquazi, L. Caspani, M. Peccianti, M. Clerici, M. Ferrera, L. Razzari, D. Duchesne, B. E. Little, S. T. Chu, D. J. Moss, and R. Morandotti, "Self-locked optical parametric oscillation in a CMOS compatible microring resonator: a route to robust optical frequency comb generation on a chip," Opt. Express **21**, 13333–13341 (2013).
36. D. G. Rabus and C. Sada, "Ring resonators: theory and modeling," in *Integrated Ring Resonators* (Springer, 2020), p. 9.
37. T. Fessant, "Theoretical investigation of threshold properties of purely and partly gain-coupled distributed feedback semiconductor lasers with stepwise constant coupling coefficients," J. Opt. Soc. Am. B **15**, 2689–2699 (1998).
38. Purnawirman, E. S. Magden, G. Singh, N. Singh, A. Baldycheva, E. S. Hosseini, J. Sun, M. Moresco, T. N. Adam, G. Leake, D. Coolbaugh, J. D. B. Bradley, and M. R. Watts, "Ultra-narrow-linewidth Al_2O_3:Er^{3+} lasers with a wavelength-insensitive waveguide design on a wafer-scale silicon nitride platform," Opt. Express **25**, 13705–13713 (2017).
39. W. A. P. M. Hendriks, L. Chang, C. I. van Emmerik, J. Mu, M. de Goede, M. Dijkstra, and S. M. Garcia-Blanco, "Rare-earth ion doped Al_2O_3 for active integrated photonics," Adv. Phys. X **6**, 1833753 (2020).
40. J. Y. Suh, C. H. Kim, W. Zhou, M. D. Huntington, D. T. Co, M. R. Wasielewski, and T. W. Odom, "Plasmonic Bowtie nanolaser arrays," Nano Lett. **12**, 5769–5774 (2012).
41. F. van Beijnum, P. J. van Veldhoven, E. J. Geluk, M. J. A. de Dood, G. W. 't Hooft, and M. P. van Exter, "Surface plasmon lasing observed in metal hole arrays," Phys. Rev. Lett. **110**, 206802 (2013).
42. D. Wang, A. Yang, W. Wang, Y. Hua, R. D. Schaller, G. C. Schatz, and T. W. Odom, "Band-edge engineering for controlled multi-modal nanolasing in plasmonic superlattices," Nat. Nanotechnol. **12**, 889–894 (2017).
43. P. Marin-Palomo, J. N. Kemal, M. Karpov, A. Kordts, J. Pfeifle, M. H. P. Pfeiffer, P. Trocha, S. Wolf, V. Brasch, M. H. Anderson, R. Rosenberger, K. Vijayan, W. Freude, T. J. Kippenberg, and C. Koos, "Microresonator-based solitons for massively parallel coherent optical communications," Nature **546**, 274–279 (2017).
44. J. Brendel, E. Mohler, and W. Martienssen, "Time-resolved dual-beam two-photon interferences with high visibility," Phys. Rev. Lett. **66**, 1142–1145 (1991).
45. J. Lehmann, M. Merschdorf, W. Pfeiffer, A. Thon, S. Voll, and G. Gerber, "Surface plasmon dynamics in silver nanoparticles studied by femtosecond time-resolved photoemission," Phys. Rev. Lett. **85**, 2921–2924 (2000).
46. D. Peceli, S. Webster, D. A. Fishman, C. M. Cirloganu, H. Hu, O. V. Przhonska, V. V. Kurdyukov, Y. L. Slominsky, A. I. Tolmachev, A. D. Kachkovski, R. R. Dasari, S. Barlow, S. R. Marder, D. J. Hagan, and E. W. Van Stryland, "Optimization of the double pump-probe technique: decoupling the triplet yield and cross section," J. Phys. Chem. A **116**, 4833–4841 (2012).
47. T. P. H. Sidiropoulos, R. Röder, S. Geburt, O. Hess, S. A. Maier, C. Ronning, and R. F. Oulton, "Ultrafast plasmonic nanowire lasers near the surface plasmon frequency," Nat. Phys. **10**, 870–876 (2014).
48. D. Cao, M. Li, J. Zhu, Y. He, T. Chen, Y. Liu, M. Chen, and Y. Yang, "Enhancement of photoelectrochemical performance in ferroelectric films via the introduction of an Au buffer layer," J. Semicond. **42**, 112701 (2021).
49. Z. Zheng, X. Wang, Y. Shen, Z. Luo, L. Li, L. Gan, Y. Ma, H. Li, A. Pan, and T. Zhai, "Space-confined synthesis of 2D all-inorganic $CsPbI_3$ perovskite nanosheets for multiphoton-pumped lasing," Adv. Opt. Mater. **6**, 1800879 (2018).
50. M. T. Hill and M. C. Gather, "Advances in small lasers," Nat. Photonics **8**, 908–918 (2014).
51. Z. Y. Wu, J. Chen, Y. Mi, X. Y. Sui, S. A. Zhang, W. N. Du, R. Wang, J. Shi, X. X. Wu, X. H. Qiu, Z. Z. Qin, Q. Zhang, and X. F. Liu, "All-inorganic $CsPbI_3$ nanowire based plasmonic lasers," Adv. Opt. Mater. **6**, 1800674 (2018).